Hindawi
Journal of Sensors
Volume 2020, Article ID 8849618, 11 pages
https://doi.org/10.1155/2020/8849618

*Research Article*

# Underground Communications Using Capacitive Data Transfer Devices

**Shaoge Zang, Keran Hou, and Sing Kiong Nguang**

*Department of Electrical, Computer, and Software Engineering, The University of Auckland, 1010, New Zealand*

Correspondence should be addressed to Shaoge Zang; szan145@aucklanduni.ac.nz

Received 23 April 2020; Revised 3 August 2020; Accepted 15 August 2020; Published 15 September 2020

Academic Editor: Christos Riziotis

Copyright © 2020 Shaoge Zang et al. This is an open access article distributed under the Creative Commons Attribution License, which permits unrestricted use, distribution, and reproduction in any medium, provided the original work is properly cited.

This paper explores the feasibility of applying the capacitive power transfer (CPT) technology in underground data transmission applications. Based on the electrical properties of soils, the paper extends the existing CPT air coupler model into a more generalized model. The autonomous push-pull inverter is selected to power the CPT system and modified to further the data transmission range. With a designed load shift keying (LSK) circuitry, this self-oscillating inverter regards the data as a sequence of impedance changes, resulting in operation frequency drifts. A Frequency Shift Keying (FSK) demodulator is applied to capture the frequency variations and recover back to data. The proposed design has been simulated, verified, and implemented on a complete prototype. Various testings have been carried out, and the results are satisfactory.

## 1. Introduction

Smart farming and precision agriculture are drawing increasing popularity over the last several years. This new farming concept integrates the Internet of Things (IoT) to improve harvest productivity with a more sustainable farming practice [1, 2]. Underground sensors then have been widely used and developed to accommodate the needs. The sensors play an essential role in monitoring soil nutrition levels, water concentrations, environmental hazards, etc.

With a massive sensor deployment scale, data collection can be challenging. Rather than using physical wire to connect between sensors for retrieving data, wireless communication is a sensible option in favour of its flexibility and convenience. It allows users to do real-time monitoring on the plants and the sensors. Nevertheless, data transfer through soils could be a difficult task. Conventional Radio Frequency (RF) modules are not suitable for underground communications as the signal can be highly attenuated due to the electrical properties of soils (e.g., electrical conductivity and electrical permittivity) [3]. Moreover, the texture of soils can be primarily affected by weather, geographical locations, insects, etc., leading to a worse performance [4].

Currently, two technologies are mostly applied in the underground communications: electromagnetic wave (EM) and Magnetic Induction (MI) [5–7]. The working principle of EM technology is the same as RF modules. It uses a much lower frequency to minimize the path loss due to the soil electrical properties. The performance and flexibility of the EM technology are limited to its relatively high-power consumption and antenna sizes [8, 9]. In another study, MI uses a pair of inductively coupled coils to transmit the data. The magnetic fields generated by the transmitting coil will induce a voltage on the receiving end [10]. The performance of MI is heavily dependent on the alignment of the coils. The coils need to be aligned face to face perfectly to get maximum transmission range [5].

CPT is an alternative method to achieve wireless power transfer (WPT) and data transfer [11]. A standard CPT system has four metal plates to form a capacitive coupling. The power is transferred between the plates via electric fields. Compared to the MI technology, CPT systems have advantages in terms

of lightweight and low cost [12, 13]. They barely suffer from eddy current losses in high-frequency magnetic fields when there is metallic material nearby [14]. Besides, the CPT systems are found to have a better misalignment performance [15, 16]. Several research groups have already attempted to use CPT to achieve data transmission in some industrial applications [17, 18]. Compared to the EM technology, the CPT system can be more energy-efficient and easier to design. With proper designs, it can achieve both wireless data and power delivery [19], which can significantly extend the battery life.

Motivated by merits of the CPT technology, this paper explores the feasibility to apply the CPT in underground data transmission. This paper modifies the current air capacitor coupler model in studies [17–19] into a more generalized underground impedance coupler model to describe the electrical characteristics of soils. Based on the modified model, we introduced load shift keying (LSK) circuitry on the sensor side. The data then can be modulated by switching a load on the sensor side, causing an impedance change to the system. Due to the unique working principle of the push-pull inverter, the impedance change will result in an inverter operation frequency drift. These frequency variations are captured by Frequency Shift Keying (FSK) circuitry on the receiving end and recovered into data. In such way, the battery life of sensors can be extensively increased as they only consume a small amount of current to drive the load switch. An additional transformer is used in the push-pull inverter to boost up the output voltage, which further improves the data transmission range. Besides, the transformer replaces the resonant component in the inverter topology and makes it more compact. A comprehensive system circuit model is built and simulated. The performance of the proposed CPT data transfer system has been tested under various conditions. The experimental results indicate a promising sign.

The main contribution of this paper can be summarized as follows:

(i) Analyze the soil electrical properties and extend the standard CPT model to a more generalized model

(ii) Build a comprehensive circuit simulation model of the push-pull inverter that incorporates the soil electrical properties

(iii) Achieve underground data transfer via FSK modulation with the push-pull inverter

The paper is structured as follows: In Section 1, the difference between the air coupler model and the underground coupler model is presented in the simulation. A more generalized circuit model is derived based on existing studies. Section 2 elaborates the proposed CPT data transfer system based on the push-pull inverter. In Section 3, multiple testings have been carried out, and the experiment results are presented. The conclusion is drawn in Section 4.

## 2. Underground Impedance Coupler Model

In this section, the underground coupler setup is presented. With the same coupler setup, the authors firstly compare the electrical property difference of using air and soils as the mediums. The results are simulated and visualized in the electromagnetic software CST. Based on the simulation results, the paper modifies the current air coupler model to a more generalized model to suit the proposed application.

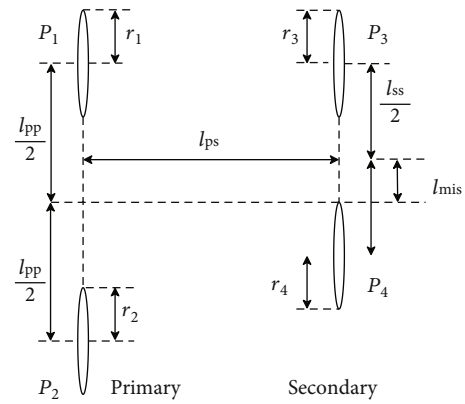


Figure 1: Demonstration of the plate arrangements.

*2.1. Underground Plate Configuration.* The underground impedance coupler configuration is illustrated in Figure 1. A standard four-plate CPT system is used in this paper. The radius of each plate is labelled as $r_i$, where $i = 1, 2, 3, 4$. Two round plates $P_1$ and $P_2$ are placed on the primary side, and the distance between two primary plates is marked as $l_{pp}$. Similarly, $l_{ss}$ is the distance between $P_3$ and $P_4$ on the secondary side. The lateral distance between the two sides is tagged as $l_{ps}$. The misalignment $l_{mis}$ is the difference between two midpoints of $l_{pp}$ and $l_{ss}$.

Soil is commonly known to be conductive and can be modelled as an infinite amount of capacitive and conductive lumped elements $R_{lumped}$ and $C_{lumped}$ connected in parallel. Ignoring the fringing effect, the impedance of every "lump" of a cross-sectional area of $\delta A$ and a length of $\delta d$ can be approximated as

$$Z_{lump} = \frac{\delta d}{\delta A\, \sigma\, \varepsilon_r\, \varepsilon_0\, s\, (1/\sigma + 1/\varepsilon_r\, \varepsilon_0\, s)}, \quad (1)$$

where $s = 2\pi f j$, $\varepsilon_0 = 8.854 \times 10^{-12}$ F/m, $\varepsilon_r$ is the relative permittivity, and $\sigma$ is the conductivity of the dielectric medium.

Simulation has been conducted in the CST software. CST is a high-performance 3D electromagnetic analysis software package for designing, analyzing, and optimizing electromagnetic components and systems [20]. The soil property was set from the source [21], where silty soil with 30% water content was chosen. Two identical round metal plates with diameters of 7 cm are placed 7 cm away from each other. A sinusoidal excitation voltage of 1 MHz is applied to one of the plates.

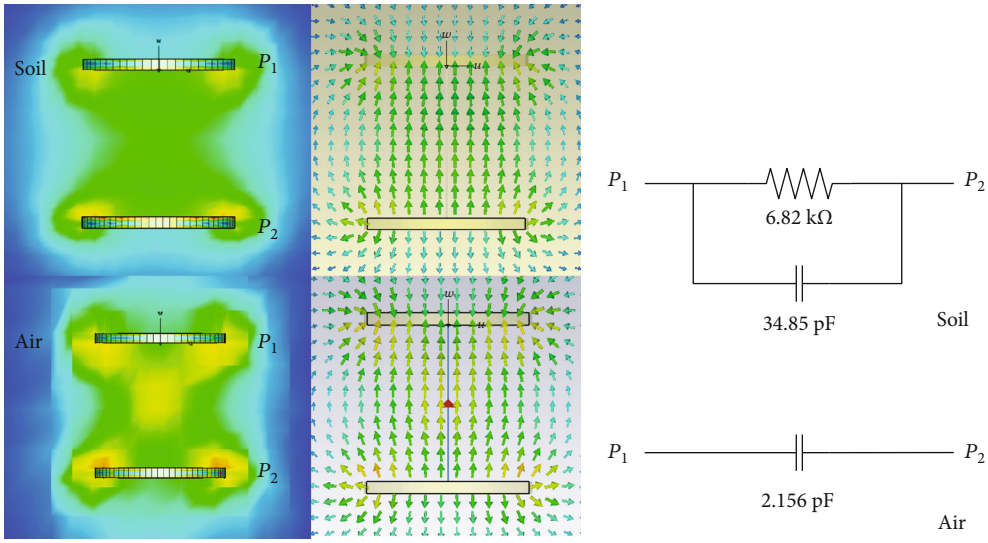


(a) E-field distributions (b) Equivalent circuit models

Figure 2: CST simulation results.

Table 1: CST simulation results.

| Medium | Frequency | Capacitance | Resistance | Reactance | Impedance | Phase |
|---|---|---|---|---|---|---|
| Air | 1 MHz | 2.156 pF | 0 Ω | 73.8 kΩ | 73.8 kΩ | -1.57 rad |
| Soil | 1 MHz | 34.85 pF | 6.82 kΩ | 4.57 kΩ | 3.795 kΩ | -0.981 rad |

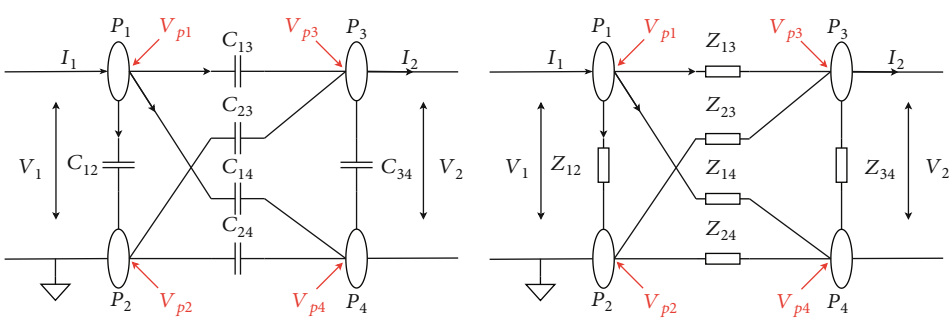


(a) Original coupler model (b) Improved coupler model for soils

Figure 3: Coupler model.

Figure 2 shows the electric field distributions of couplers with air and soils as the medium and their equivalent circuit models. Simulation results are summarized in Table 1.

From Table 1, it can be seen that the air coupler is purely capacitive with an impedance of 73.8 kΩ. On the contrary, with soil as the medium, the resulting impedance is of 3.795 kΩ at −0.981 radians. It is equivalent to a resistor of 6.82 kΩ and a capacitor of 34.85 pF connected in parallel.

The soil behaves as a lossy dielectric. The real part of dielectric constant contributes to the capacitive reactance of soil while the imaginary dielectric constant is the loss. The standard air coupler model in current CPT studies cannot be applied and needs modifications.

*2.2. Improved Underground Coupler Model for Soil Condition.* In current CPT studies, the air couplers are modelled by introducing the capacitors between any two plates. With four plates, it forms a network with six capacitors. We improved the original model by replacing capacitors with corresponding impedances, as depicted in Figure 3. The impedance has both the resistive part and the capacitive part to describe the electrical characteristics of the soils.

To analyze the circuits in Figure 3, we define $V_{p1}$, $V_{p2}$, $V_{p3}$, and $V_{p4}$ as the voltages on each plate, respectively. Set $V_{p2} = 0$ as the electrical reference and apply Kirchhoff's current law (KCL), the following equations could be obtained:

$$I_1 = \frac{V_{p1} - V_{p2}}{Z_{12}} + \frac{V_{p1} - V_{p3}}{Z_{13}} + \frac{V_{p1} - V_{p4}}{Z_{14}},$$
$$I_2 = \frac{V_{p3} - V_{p4}}{Z_{34}} + \frac{V_{p3} - V_{p2}}{Z_{23}} - \frac{V_{p1} - V_{p3}}{Z_{13}}. \quad (2)$$

Since $V_1 = V_{p1} - V_{p2}$ and $V_2 = V_{p3} - V_{p4}$, the transfer function of $V_2/V_1$ can be derived:

$$H_{1,2} = \frac{Z_{12}\left(Z_{23}Z_{14} - Z_{13}Z_{24}\right)}{Z_{D1}}, \tag{3}$$

where

$$\begin{aligned} Z_{D1} = {} & Z_{13}Z_{23}Z_{14} + Z_{13}Z_{23}Z_{24} + Z_{13}Z_{14}Z_{24} \\ & + Z_{13}Z_{23}Z_{12} + Z_{23}Z_{14}Z_{24} + Z_{13}Z_{24}Z_{12} \\ & + Z_{23}Z_{14}Z_{12} + Z_{14}Z_{24}Z_{12}. \end{aligned} \tag{4}$$

The input impedance $Z_{\text{in,pri}} = V_1/I_1$ can be expressed as

$$Z_{\text{in,pri}} = \frac{Z_{12}(Z_{13}Z_{14}Z_{23} + Z_{13}Z_{14}Z_{24} + Z_{13}Z_{23}Z_{24} + Z_{13}Z_{14}Z_{34} + Z_{14}Z_{23}Z_{24} + Z_{13}Z_{24}Z_{34} + Z_{14}Z_{23}Z_{34} + Z_{23}Z_{24}Z_{34})}{Z_{12}Z_{13}Z_{23} + Z_{12}Z_{13}Z_{24} + Z_{12}Z_{14}Z_{23} + Z_{12}Z_{14}Z_{24} + Z_{13}Z_{14}Z_{23} + Z_{13}Z_{14}Z_{24} + Z_{12}Z_{13}Z_{34} + Z_{12}Z_{14}Z_{34} + Z_{13}Z_{23}Z_{24} + Z_{13}Z_{14}Z_{34} + Z_{14}Z_{23}Z_{24} + Z_{12}Z_{23}Z_{34} + Z_{12}Z_{24}Z_{34} + Z_{13}Z_{24}Z_{34} + Z_{14}Z_{23}Z_{34} + Z_{23}Z_{24}Z_{34}}. \tag{5}$$

It should be noticed that the impedance network is no longer linear. Therefore, the reciprocal principle for a two-port system cannot be applied. In other words, $H_{1,2} \neq H_{2,1}^{-1}$. The transfer function of $V_1/V_2$ can be expressed as

$$H_{2,1} = \frac{Z_{34}\left(Z_{14}Z_{23} - Z_{13}Z_{24}\right)}{Z_{D2}}, \tag{6}$$

where

$$\begin{aligned} Z_{D2} = {} & Z_{13}Z_{14}Z_{23} + Z_{13}Z_{14}Z_{24} + Z_{13}Z_{23}Z_{24} \\ & + Z_{13}Z_{14}Z_{34} + Z_{14}Z_{23}Z_{24} + Z_{13}Z_{24}Z_{34} \\ & + Z_{14}Z_{23}Z_{34} + Z_{23}Z_{24}Z_{34}. \end{aligned} \tag{7}$$

The input impedance on the secondary side $Z_{\text{in,sec}}$ is described as

$$Z_{\text{in,sec}} = \frac{Z_{34}(Z_{13}Z_{23}Z_{14} + Z_{13}Z_{23}Z_{24} + Z_{13}Z_{14}Z_{24} + Z_{13}Z_{23}Z_{12} + Z_{14}Z_{23}Z_{24} + Z_{12}Z_{13}Z_{24} + Z_{12}Z_{14}Z_{23} + Z_{12}Z_{14}Z_{24})}{Z_{13}Z_{14}Z_{34} + Z_{13}Z_{24}Z_{34} + Z_{14}Z_{23}Z_{34} + Z_{23}Z_{24}Z_{34} + Z_{13}Z_{14}Z_{23} + Z_{13}Z_{23}Z_{24} + Z_{12}Z_{13}Z_{34} + Z_{12}Z_{23}Z_{34} + Z_{13}Z_{14}Z_{24} + Z_{12}Z_{13}Z_{23} + Z_{14}Z_{23}Z_{24} + Z_{12}Z_{14}Z_{34} + Z_{12}Z_{24}Z_{34} + Z_{12}Z_{13}Z_{24} + Z_{12}Z_{14}Z_{23} + Z_{12}Z_{14}Z_{24}}. \tag{8}$$

Similar to the analysis in study [16], the circuit is simplified into an equivalent $\pi$ model as shown in Figure 4. As the model is asymmetrical, the components $Z_{M1}$, $Z_{M2}$, $Z_{\text{int }1}$, and $Z_{\text{int }2}$ need to be considered separately. The input impedance can be described as

$$\begin{aligned} Z_{\text{in,pri}} &= \frac{Z_{\text{int }1}\left(Z_{M1} + Z_{M2} + Z_{\text{int }2}\right)}{Z_{M1} + Z_{M2} + Z_{\text{int }1} + Z_{\text{int }2}}, \\ Z_{\text{in,sec}} &= \frac{Z_{\text{int }2}\left(Z_{M1} + Z_{M2} + Z_{\text{int }1}\right)}{Z_{M1} + Z_{M2} + Z_{\text{int }1} + Z_{\text{int }2}}. \end{aligned} \tag{9}$$

The transfer functions can be expressed as

$$H_{1,2} = \frac{Z_{\text{int }2}}{Z_{M1} + Z_{M2} + Z_{\text{int }2}}, \tag{10}$$

$$H_{1,2} = \frac{Z_{\text{int }2}}{Z_{M1} + Z_{M2} + Z_{\text{int }2}}. \tag{11}$$

By solving Equations (3)–(11), the component value in the $\pi$ model can be obtained:

$$\begin{aligned} Z_M &= \frac{Z_{13}Z_{14}Z_{23} + Z_{13}Z_{14}Z_{24} + Z_{13}Z_{23}Z_{24} + Z_{14}Z_{23}Z_{24}}{Z_{14}Z_{23} - Z_{13}Z_{24}}, \\ Z_{\text{int }1} &= \frac{Z_{12}(Z_{13}Z_{14}Z_{23} + Z_{13}Z_{14}Z_{24} + Z_{13}Z_{23}Z_{24} + Z_{14}Z_{23}Z_{24})}{Z_{12}Z_{13}Z_{23} + 2Z_{12}Z_{13}Z_{24} + Z_{12}Z_{14}Z_{24} + Z_{13}Z_{14}Z_{23} + Z_{13}Z_{14}Z_{24} + Z_{13}Z_{23}Z_{24} + Z_{14}Z_{23}Z_{24}}, \\ Z_{\text{int }2} &= \frac{Z_{34}(Z_{13}Z_{14}Z_{23} + Z_{13}Z_{14}Z_{24} + Z_{13}Z_{23}Z_{24} + Z_{14}Z_{23}Z_{24})}{Z_{13}Z_{14}Z_{23} + Z_{13}Z_{14}Z_{24} + Z_{13}Z_{23}Z_{24} + Z_{13}Z_{14}Z_{34} + Z_{14}Z_{23}Z_{24} + 2Z_{13}Z_{24}Z_{34} + Z_{23}Z_{24}Z_{34}}, \end{aligned} \tag{12}$$

where $Z_M = Z_{M1} + Z_{M2}$.

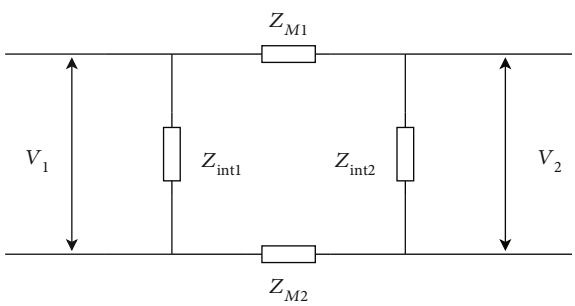


Figure 4: $\pi$ model for underground couplers.

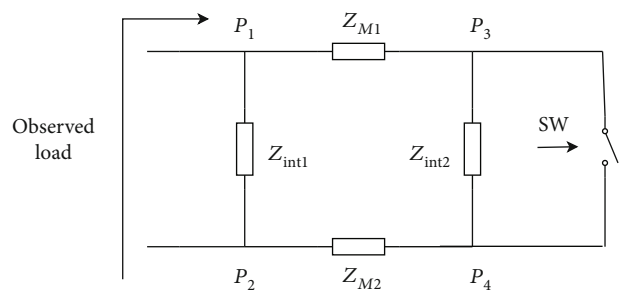


Figure 5: Load shift keying (LSK) circuitry.

## 3. Capacitive Data Transfer System Based on Push-Pull Inverter

In this section, the top to down system design is elaborated. The load shift keying circuitry is firstly presented to illustrate the effect of the load change on the underground coupler impedance. Then, the mechanism of the push-pull inverter is briefly discussed, and modifications have been made to improve the design. The proposed system design is verified by simulations using MATLAB Simulink.

*3.1. Load Shift Keying (LSK) Circuitry.* The diagram of LSK circuitry is shown in Figure 5. The microcontroller inside the sensor unit collects the data and controls the MOSFET switch. The high and low signal states of the data can be represented by the open and closed states of the switch, respectively. When the switch is closed, plate 3 and plate 4 are connected. In this case, the secondary side is shorted, and the primary side can observe minimum impedance. Similarly, when the switch is in off-state, the maximum impedance occurs. The signal strength can be quantified as the percentage change in impedance between these two states. The maximum and minimum impedance can be derived as

$$\begin{aligned} Z_{\max} &= Z_{\text{int }1} \parallel (Z_{M1} + Z_{\text{int }2} + Z_{M2}), \\ Z_{\min} &= Z_{\text{int }1} \parallel (Z_{M1} + Z_{M2}). \end{aligned} \tag{13}$$

Hence, the percentage of impedance change can be obtained as

$$\begin{aligned} \Delta Z &= \frac{Z_{\max} - Z_{\min}}{Z_{\min}} \times 100\% \\ &= \frac{Z_{\text{in,pri}} Z_{\text{in,sec}}}{(Z_{M1} + Z_{M2})\left(Z_{M1} + Z_{M2} + Z_{\text{in,pri}} + Z_{\text{in,sec}}\right)}. \end{aligned} \tag{14}$$

The simulation has been conducted in CST to visualize the electric field distributions as well as to calculate the impedance. As shown in Figure 6, the top two round metal plates are placed on the surface. The voltage difference ($V_1$) is set to 1 V. The bottom two plates are buried in the soil. It can be seen that under the short-circuited scenario and open-circuited scenario, the electric field distributions are different. When the secondary side is shorted, the electric field gets attracted to the secondary plates, and the field strength between the secondary plates becomes weaker. A probe is inserted to measure the input current ($I_1$) and the secondary plate voltage difference ($V_2$). The input impedance $Z_{\text{in}}$ can then be calculated as $Z_{\text{in}} = V_1/I_1$. The simulation results are summarized in Table 2.

It could be found that under short-circuit condition and open-circuit conditions, the observed input impedance has a small difference. With proper filter designs, the difference can be amplified to a detectable level.

### 3.2. Push-Pull Transformer FSK System

*3.2.1. Push-Pull Circuit Modelling.* The autonomous push-pull inverter was firstly introduced by Hu and Abdolkhani [22]. It converts a DC voltage source into a high-frequency AC source. Compared to other inverter topologies, this topology has significant advantages for its simplicity and high efficiency. The push-pull inverter can always ensure soft-switching during the operation, minimizing the switching loss of the transistors and electromagnetic interference (EMI). In Figure 7, it shows a CPT system with the autonomous push-pull converter. The controller does not require any external controllers and makes it more economical to use.

The operation frequency of the autonomous push-pull controller is determined by the resonant components $L_r$ and $C_r$ in the parallel tank. When the system is operating under the design frequency, it has the following relationship:

$$\omega = \frac{1}{\sqrt{L_r C_r}} = \frac{1}{\sqrt{L_s C_s}}, \tag{15}$$

where $C_s$ is the equivalent coupling capacitance, $C_s = C_{s1} C_{s2}/(C_{s1} + C_{s2})$.

The operation frequency of the push-pull inverter can be easily affected by the load. If the load has the capacitive component, the operation frequency will be lower than the designed value. Meanwhile, if the load has the inductive component, the operation frequency will be higher. The load impedance change caused by the LSK circuitry will lead to two different operation frequencies. By this unique feature, the high state and the low states of the data can then be expressed as the conditions of the switch.

The performance of the autonomous push-pull converter is limited by its output voltage. Without additional circuits, the output voltage across the parallel resonant tank is bounded by $\pi V_{\text{DC}}$. A transformer is used to level up the

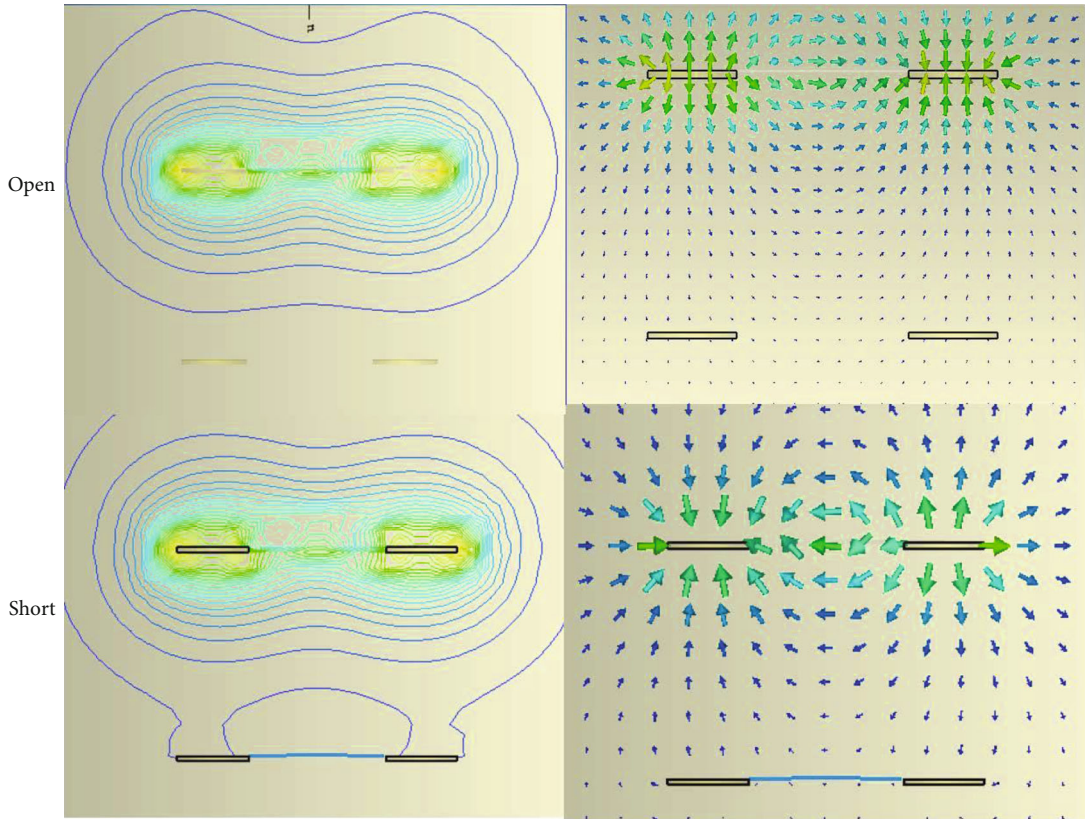


Figure 6: E-field distribution with short-circuit and open-circuit.

Table 2: Measurements from CST simulations.

| | $V_1$ (V) | $V_2$ (V) | $H_{1,2}$ | $I_1$ (mA) | $Z_{in}$ ($\Omega$) |
|---|---|---|---|---|---|
| Short-circuit | 1 | 0.03 | 0.03 | 0.2542 | 3930 |
| Open-circuit | 1 | 0.03 | 0.03 | 0.2542 | 3933 |

voltage. As depicted in Figure 8, the Tee model of the transformer is applied to analyze the circuit. The magnetization inductance $L_M$ can be used to replace the resonant inductor $L_r$ to further reduce the converter size.

As the system is running at the megahertz region, the nonideal properties of the transformer also need to be considered. The leakage inductance on the primary side and secondary side is described as $L_{11}$ and $L_{22}$, respectively. Additional capacitor $C_T$ is used to compensate the leakage inductance $L_{22}$ to achieve maximum sensitivity. In other words, the operation frequency of the push-pull inverter will only vary when the load impedance changes. No compensation is needed for $L_{11}$ as the step-up transformer has a much lower primary inductance compared to $L_{22}$.

The simulation model has been structured using the MATLAB Simscape package as shown in Figure 9. The transformer is set to have a turn ratio $\alpha = 3$ with a coupling factor $k_c$ of 0.8. The MOSFET parameters are imported from nominal values of a fast-switching MOSFET, IRF510. A square wave signal is applied to the switch to mimic the data transfer. Detailed simulation parameters are attached in Table 3.

As shown in Figure 10(b), the output voltage of the push-pull inverter has an amplitude of around 18.5 V, which is close to $\pi V_{DC}$. After the transformer, the voltage is boosted up to 52.5 V. The voltage gain is close to the designed turns ratio. It can also be seen from Figure 10(d) that when the switching signal is applied, the operation frequency can change slightly from 1.082 MHz to 1.086 MHz.

*3.2.2. System Design.* As discussed above, the operation frequency of the push-pull inverter will change automatically when the observed impedance changes. This paper utilizes this feature and designs an FSK demodulator based on Phase Lock Loop (PLL). Figure 11 illustrates the overall system diagram.

An extra winding is firstly used on the transformer to step down the push-pull inverter output voltage to a detectable analogue voltage. This lowered voltage is fed into the phase comparator and compared with the signal generated by the voltage-controlled oscillator (VCO). The phase comparator output signal will then be filtered. As the input analogue voltage frequency changes, the amplitude of this signal will vary correspondingly. The variations are captured and recovered to the data using cascaded filters and processed by a programmable system-on-chip (PSoC).

## 4. Experimental Results

Figure 12 shows the experiment setup. A 70-litre container filled with soils is used to simulate the ground condition.

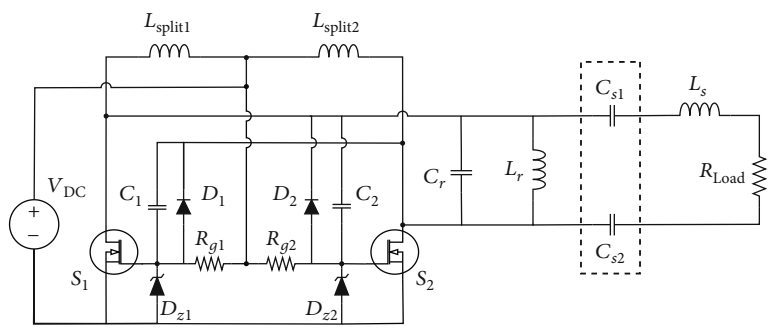


Figure 7: CPT system based on the improved autonomous push-pull inverter.

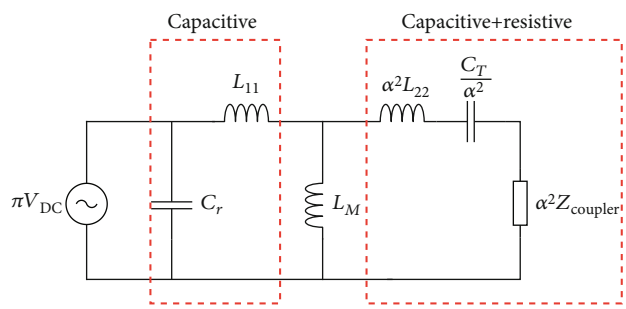


Figure 8: Simplified circuit diagram for a push-pull inverter with a nonideal transformer.

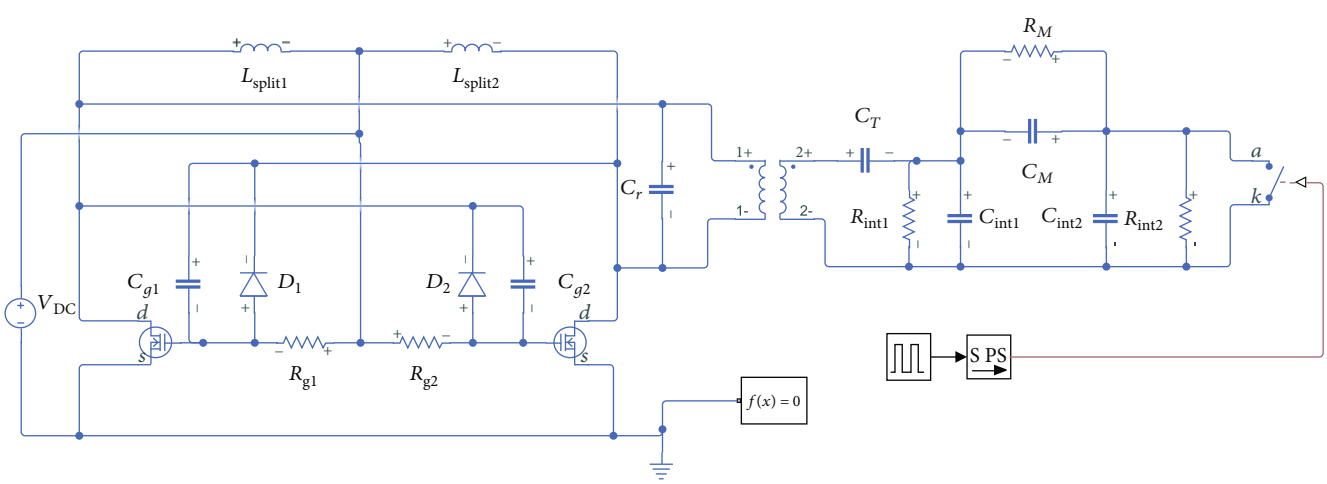


Figure 9: MATLAB simulation model.

Table 3: Simulation parameters.

| Parameter | Values | Parameter | Values |
|---|---|---|---|
| $L_1, L_2$ | 680 $\mu$H | $R_1, R_2$ | 150 $\Omega$ |
| $C_1, C_2$ | 140 pF | $k_c$ | 0.8 |
| $L_{T,p}$ | 30 $\mu$H | $L_{T,s}$ | 270 $\mu$H |
| $C_r$ | 500 pF | $C_T$ | 367 pF |
| $V_{DC}$ | 6 V | $\alpha$ | 3 |

On the left side, the sensor unit uses a STM32 microcontroller to transmit data continuously, powered by a 9 V battery. On the right side, the push-pull inverter is connected with an auxiliary power supply. A probe is connected to monitor the VCO input voltage. The voltage signal is also fed into a PSoC5 microcontroller to convert back into a UART data string and displayed on a PC screen. The baud rate is set to 9600.

All component values are included in Table 4. The leakage inductance of the transformer properties is preverified by undertaking short-circuit and open-circuit tests under the operation frequency of 1 MHz. It should be noted that the value of $C_r$ is smaller than the one used in the simulation. This is because the output capacitance of the MOSFETs contributes to $C_r$ as well.

The experiments were conducted under the configuration shown in Figure 1. In the setup, we assume that the

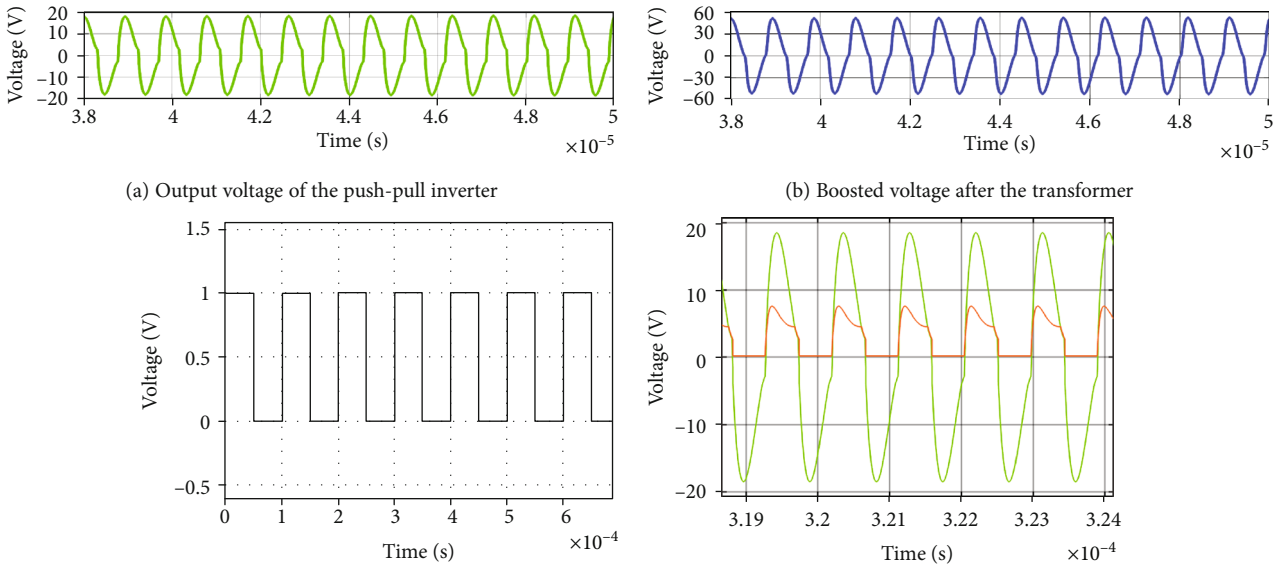


(a) Output voltage of the push-pull inverter

(b) Boosted voltage after the transformer

(c) Switching signal

(d) Resulting frequency variation

Figure 10: Simulation results.

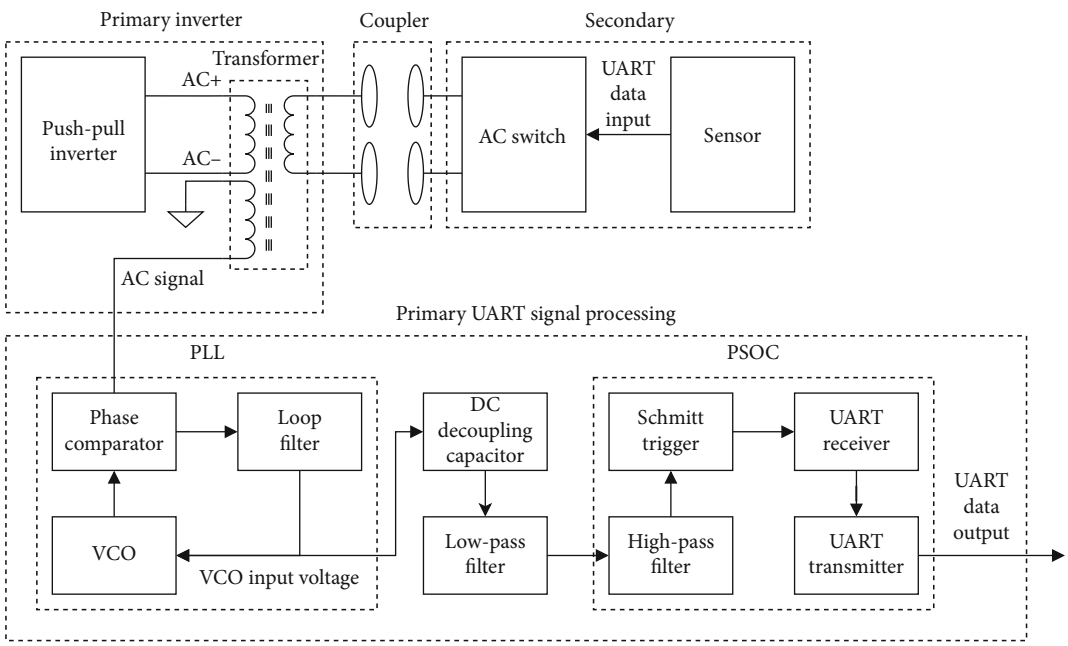


Figure 11: CPT data transfer system based on push-pull inverter.

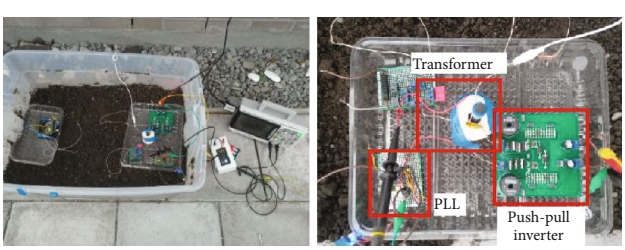


Figure 12: Experiment setup.

Table 4: Experiment component parameters.

| Parameter | Values | Parameter | Values |
|---|---|---|---|
| $L_1, L_2$ | 680 $\mu$H | $R_1, R_2$ | 150 $\Omega$ |
| $C_1, C_2$ | 140 pF | $k_c$ | 0.8 |
| $L_{T,p}$ | 30 $\mu$H | $L_{T,s}$ | 270 $\mu$H |
| $C_r$ | 243 pF | $C_T$ | 330 pF |
| $V_{DC}$ | 6 V | $\alpha$ | 3 |
| PLL | CD4046BE | MOSFET | IRF510 |

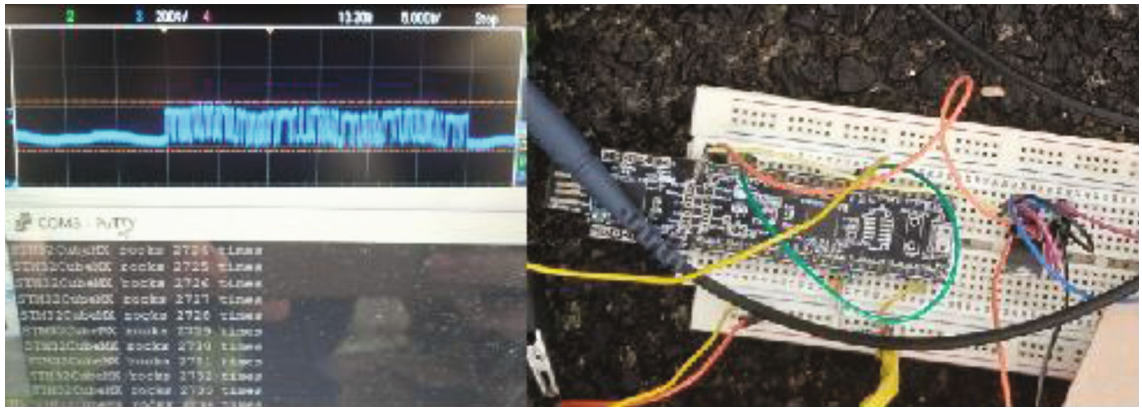

Figure 13: Data transmission experiment.

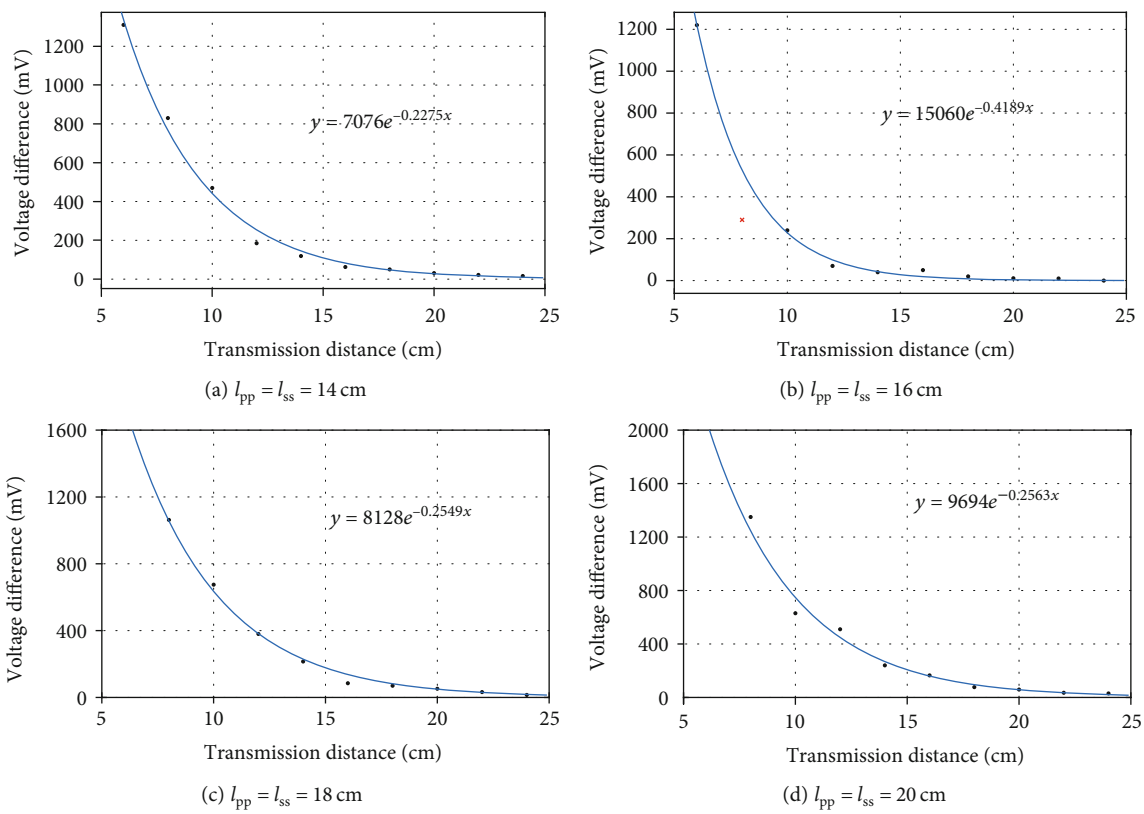


Figure 14: Signal strength under different lateral distances.

longitudinal distance $l_{pp} = l_{ss} = 12$ cm; thus, $l_{mis}$ is equal to 0. The lateral distance $l_{ps} = 12$ cm.

As shown in Figure 13, the VCO output voltage was captured with native Keysight desktop application. After filtering the signal, the emulator application "PuTTY" was able to recognise the signal and converted into original data. The data was sent at a baud rate of 9600 in every 0.5 s, and the system was able to run continuously over a long time.

The signal strength was measured in terms of the AC signal amplitude. With a fixed longitudinal distance, multiple testings have been conducted to test the maximum lateral transmission distance. As shown in Figure 14, all signal strength curves follow an exponential decay. With an increasing lateral distance, the voltage differences drop dramatically and become much harder to detect.

Similar testings have also been conducted to find the maximum longitudinal distance. The results are illustrated in Figure 15. During the experiments, the maximum data transfer range is found around $1.2l_{ps}$ with no bit error rate (BER). It should be noticed that under that same lateral distance, the voltage difference will be more significant with a longer longitudinal distance. Less electric fields are attracted to the horizontal plate, resulting in a smaller cross-coupling capacitance between the two primary plates. To get a further transmission range, the two primary plates should be placed as far as possible.

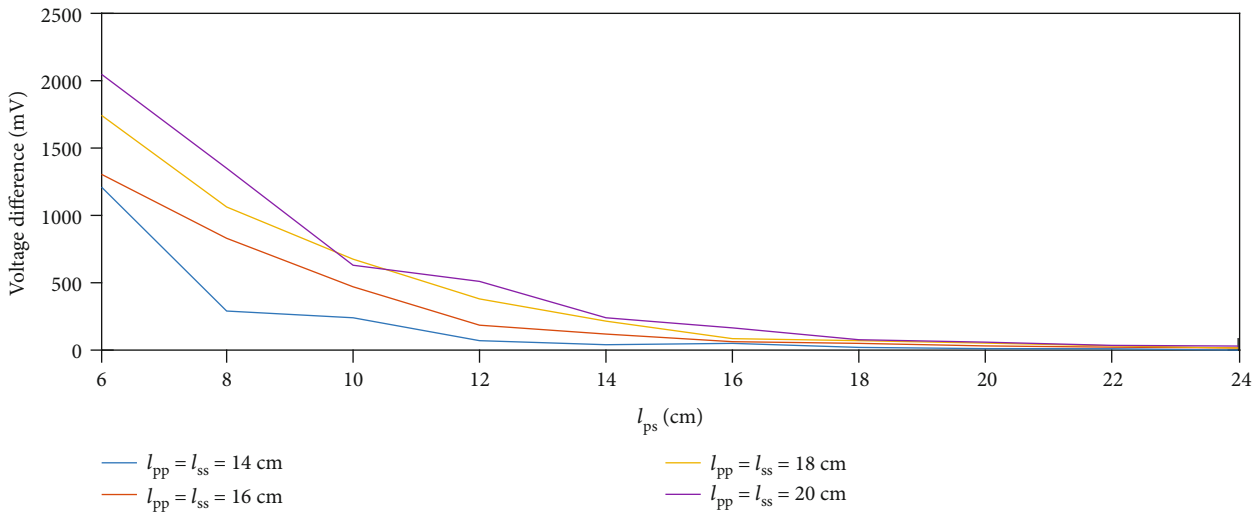


Figure 15: Signal strength under different longitudinal distances.

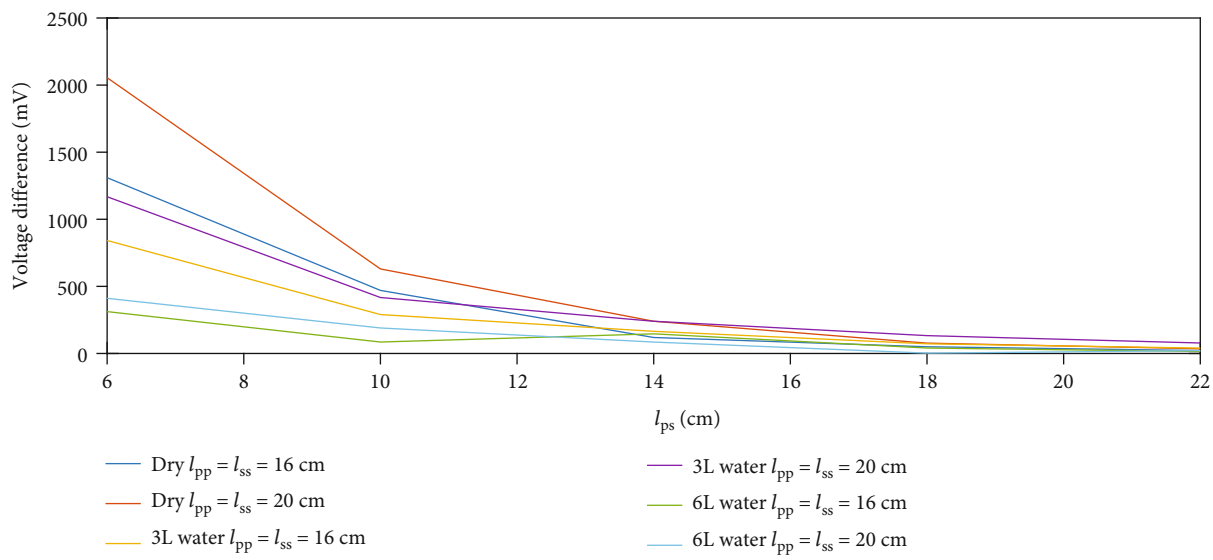


Figure 16: Signal strength under different soil moisture levels.

Additional testings have been carried out to explore the performance of this data transfer system under different soil moisture levels, as shown in Figure 16. It can be found that with the dry soils, the signal strength is the strongest. The signal strength will drop significantly as the water concentration increases. This phenomenon agrees with the studies in [3]. A higher moisture level in soils will cause additional path loss during the data transmission.

## 5. Conclusion

This paper explores the feasibility of applying capacitive power transfer technology (CPT) in an underground data transfer system. The differences of using air and soils as the medium of couplers have been explained and visualized. We have extended the current air coupler model to a more generalized expression to describe the electrical properties of soils. The push-pull inverter has been chosen to drive the CPT system, on which a transformer has been employed to increase the data transmission range. By introducing an LSK circuitry to control a switch on the sensor side, the observed load impedance will change correspondingly, leading to operation frequency variations. These variations are captured by the FSK circuitry on the receiving end and demodulated. The prototype has been implemented and tested in various working conditions. The proposed design has been proved valid and successful.

## Data Availability

No data were used to support this study.

## Conflicts of Interest

The authors declare no conflict of interest.

## Acknowledgments

This paper is dedicated as a memorial to Prof. Sing Kiong Nguang. The authors gratefully thank Prof. Sing Kiong Nguang for his guidance and support during the studies.

## References

[1] S. Pamukcu, L. Cheng, and M. Pervizpour, "Chapter 1 - introduction and overview of underground sensing for sustainable response," in *Underground Sensing*, S. Pamukcu and L. Cheng, Eds., pp. 1–42, Academic Press, 2018.

[2] I. F. Akyildiz and E. P. Stuntebeck, "Wireless underground sensor networks: research challenges," *Ad Hoc Networks*, vol. 4, no. 6, pp. 669–686, 2006.

[3] M. L. Oelze, W. D. O'Brien, and R. G. Darmody, "Measurement of attenuation and speed of sound in soils," *Soil Science Society of America Journal*, vol. 66, p. 9, 2002.

[4] A. R. Silva and M. C. Vuran, "Empirical evaluation of wireless underground-to- underground communication in wireless underground sensor networks," in *Distributed Computing in Sensor Systems*, Lecture Notes in Computer Science, B. Krishnamachari, S. Suri, W. Heinzelman, and U. Mitra, Eds., pp. 231–244, Springer, Berlin, Heidelberg, 2009.

[5] Z. Sun and I. F. Akyildiz, "Magnetic induction communications for wireless underground sensor networks," *IEEE Transactions on Antennas and Propagation*, vol. 58, no. 7, pp. 2426–2435, 2010.

[6] A. R. Silva and M. Moghaddam, "Design and implementation of low-power and mid-range magnetic-induction-based wireless underground sensor networks," *IEEE Transactions on Instrumentation and Measurement*, vol. 65, no. 4, pp. 821–835, 2016.

[7] A. Salam, M. C. Vuran, X. Dong, C. Argyropoulos, and S. Irmak, "A theoretical model of underground dipole antennas for communications in internet of underground things," *IEEE Transactions on Antennas and Propagation*, vol. 67, no. 6, pp. 3996–4009, 2019.

[8] Z. Sun, I. F. Akyildiz, and G. P. Hancke, "Dynamic connectivity in wireless underground sensor networks," *IEEE Transactions on Wireless Communications*, vol. 10, no. 12, pp. 4334–4344, 2011.

[9] X. Zhang, A. Andreyev, C. Zumpf, M. C. Negri, S. Guha, and M. Ghosh, "Invited paper: Thoreau: a fully-buried wireless underground sensor network in an urban environment," in *2019 11th International Conference on Communication Systems Networks (COMSNETS)*, pp. 239–250, Bengaluru, India, January 2019.

[10] X. Tan, Z. Sun, and I. F. Akyildiz, "Wireless underground sensor networks: MI-based communication systems for underground applications," *IEEE Antennas and Propagation Magazine*, vol. 57, no. 4, pp. 74–87, 2015.

[11] L. J. Zou, Q. Zhu, C. W. V. Neste, and A. P. Hu, "Modelling single-wire capacitive power transfer system with strong coupling to ground," *IEEE Journal of Emerging and Selected Topics in Power Electronics*, p. 1, 2019.

[12] F. Lu, H. Zhang, and C. Mi, "A review on the recent development of capacitive wireless power transfer technology," *Energies*, vol. 10, no. 11, p. 1752, 2017.

[13] B. Luo, T. Long, L. Guo, R. Dai, R. Mai, and Z. He, "Analysis and design of inductive and capacitive hybrid wireless power transfer system for railway application," *IEEE Transactions on Industry Applications*, vol. 56, no. 3, pp. 3034–3042, 2020.

[14] B. Luo, T. Long, R. Mai, R. Dai, Z. He, and W. Li, "Analysis and design of hybrid inductive and capacitive wireless power transfer for high-power applications," *IET Power Electronics*, vol. 11, no. 14, pp. 2263–2270, 2018.

[15] S. Zang, K. Lu, S. K. Nguang, and W. Sun, "Robust $H_\infty$ output feedback control of a rotary capacitive power transfer system," *IEEE Access*, vol. 7, pp. 113452–113462, 2019.

[16] F. Lu, H. Zhang, H. Hofmann, and C. Mi, "A CLLC-compensated high power and large air gap capacitive power transfer system for electric vehicle charging applications," in *2016 IEEE Applied Power Electronics Conference and Exposition (APEC)*, pp. 1721–1725, Long Beach, CA, USA, March 2016.

[17] K. Wang and S. Sanders, "Contactless USB — a capacitive power and bidirectional data transfer system," in *2014 IEEE Applied Power Electronics Conference and Exposition -APEC 2014*, pp. 1342–1347, Fort Worth, TX, USA, March 2014.

[18] E. Culurciello and A. G. Andreou, "Capacitive inter-chip data and power transfer for 3-D VLSI," *IEEE Transactions on Circuits and Systems II: Express Briefs*, vol. 53, no. 12, pp. 1348–1352, 2006.

[19] D. Maier, J. Heinrich, M. Böttigheimer, and N. Parspour, "A novel contactless capacitive energy and data transfer system," in *2018 IEEE Wireless Power Transfer Conference (WPTC)*, pp. 1–4, Montreal, QC, Canada, June 2018.

[20] CST, "CST Studio Suite 3D EM simulation and analysis software," https://www.3ds.com/products-services/simulia/products/cst-studio-suite/.

[21] R. Porretta and F. Bianchi, "Profiles of relative permittivity and electrical conductivity from unsaturated soil water content models," *Annals of Geophysics*, vol. 59, no. 3, article 0320, 2016, https://www.annalsofgeophysics.eu/index.php/Annuals/article/view/6990.

[22] A. P. Hu and A. Abdolkhani, "Improved autonomous current-fed push–pull resonant inverter," *IET Power Electronics*, vol. 7, no. 8, pp. 2103–2110, 2014.